

COMPUTATION OF RESPONSE FUNCTIONS BASED  
ON THE FREQUENCY-DOMAIN SOLUTION

CHAO GUO







Computation of Response Functions based on the  
Frequency-Domain Solution

by

© Chao Guo

St. John's, Newfoundland, Canada

B.Eng., Dalian University of Technology, China (2006)

A thesis submitted to the  
School of Graduate Studies  
in partial fulfillment of the  
requirements for the degree of  
Master of Engineering

Faculty of Engineering and Applied Science  
Memorial University of Newfoundland

May 2009

# TABLE OF CONTENTS

<b>List of Figures .....</b>	<b>iv</b>
<b>Nomenclature.....</b>	<b>vi</b>
<b>Acknowledgements .....</b>	<b>viii</b>
<b>Abstract.....</b>	<b>ix</b>
<b>1 Introduction .....</b>	<b>1</b>
1.1 Response Function .....	1
1.2 The Computation of Added Mass and Damping Coefficients .....	3
1.3 The Computation of Response Function from Frequency-Domain Results.....	4
1.4 Thesis Contents .....	5
<b>2 The Panel-Free Method for Frequency Domain Computation .....</b>	<b>7</b>
2.1 Mathematical Formulation.....	8
2.2 Geometry Representation .....	12
<b>3 Improved Transformation Method for Response Function</b>	

<b>Computation .....</b>	<b>16</b>
3.1 Mathematical Formulation.....	16
3.2 Numerical Method.....	20
3.2.1 Numerical quadratures .....	22
3.2.2 Fast Fourier Transform .....	23
3.2.3 Semi-analytical method .....	24
3.2.4 Accuracy check of the integration method.....	27
<b>4 Numerical results .....</b>	<b>29</b>
4.1 Hemisphere .....	29
4.1.1 The added mass and damping coefficients.....	30
4.1.2 Response function.....	31
4.1.3 Accuracy check of the integral method.....	32
4.2 Wigley Hull .....	34
4.2.1 Added mass and damping coefficient .....	35
4.2.2 Response function.....	37
4.2.3 Accuracy check of the integral method.....	38
4.3 Liquefied Natural Gas (LNG) Carrier.....	40
4.3.1 Added mass and damping coefficient .....	41
4.3.2 Response function.....	43
4.3.3 Accuracy check of the integral method.....	45
<b>5 Conclusions .....</b>	<b>50</b>
<b>References .....</b>	<b>52</b>

# List of Figures

Fig 2-1 Coordinate system .....	8
Fig 2-2 Mapping relationship for the computational space, the parametric space and the physical space .....	15
Fig 4-1 Heave added mass for the hemisphere .....	320
Fig 4-2 Heave damping coefficient for the hemisphere .....	31
Fig 4-3 Heave response function for the hemisphere .....	32
Fig 4-4 Reconstructed heave added mass for the hemisphere .....	33
Fig 4-5 Reconstructed heave damping coefficient for the hemisphere .....	33
Fig 4-6 Time-domain heave added mass for the hemisphere .....	34
Fig 4-7 Heave added mass for the Wigley hull .....	36
Fig 4-8 Heave damping coefficient for the Wigley hull .....	36
Fig 4-9 Heave response function for the Wigley hull .....	37
Fig 4-10 Pitch radiation response function for the Wigley hull .....	38
Fig 4-11 Reconstructed heave added mass for the Wigley hull .....	39
Fig 4-12 Reconstructed heave damping coefficient for the Wigley hull .....	39
Fig 4-13 Time-domain heave added mass for the Wigley hull .....	40
Fig 4-14 Gaussian points distribution on the hull surface and the lid of the LNG carrier ...	41

Fig 4-15 Heave added mass for the LNG carrier.....	42
Fig 4-16 Heave damping coefficient for the LNG carrier.....	42
Fig 4-17 Heave response function for the LNG carrier.....	42
Fig 4-18 Heave response function due to pitch for the LNG carrier.....	44
Fig 4-19 Pitch response function due to heave for the LNG carrier.....	44
Fig 4-20 Pitch response function for the LNG carrier.....	44
Fig 4-21 Reconstructed heave added mass for the LNG carrier.....	46
Fig 4-22 Time-domain heave added mass for the LNG carrier.....	46
Fig 4-23 Reconstructed heave damping coefficient for the LNG carrier.....	47
Fig 4-24 Reconstructed heave damping coefficient due to pitch for the LNG carrier.....	47
Fig 4-25 Reconstructed pitch damping coefficient due to heave for the LNG carrier.....	47
Fig 4-26 Reconstructed pitch damping coefficient for the LNG carrier.....	47

## Nomenclature

$A(\omega)$	added mass
$B$	beam of the hull
$B(\omega)$	damping coefficient
$C_b$	block coefficient
$F(t)$	load vector which composed by six components
$F^{(w)}(t)$	diffraction force
$F^{(r)}(t)$	radiation load on the hull
$g$	acceleration of gravity
$G_0(P, Q)$	Rankine source
$G_F(P, Q)$	Green function
$J_0$	Bessel function of zeroth order
$K(\tau)$	response function
$N_{i,p}$ and $N_{j,p}$	normalized B-spline basis functions
$P(x, y, z)$	a field point
$Q(x', y', z')$	source point
$S_b$	mean wetted surface

$V_n$	the normal velocity
$x(t)$	motion vector
$\beta$	heading angle of wave propagation relative to the x-axis
$\gamma(P)$	source distribution on the body wetted surface
$\delta$	relative least-difference
$\tilde{\epsilon}$	error
$\mu$	time-domain added mass
$\rho$	water density
$\sigma_k$	source strength
$\tau$	time
$\phi$	incident wave potential
$\omega$	wave frequency
$\Omega$	fluid domain
$\nabla$	volume displacement

## **Acknowledgements**

I wish to express my sincere thanks to my supervisor Dr. Wei Qiu, who suggested the research topic, for his encouragement, guidance and constructive discussions during the development of this thesis. Also, I appreciate the guidance from my co-supervisor Dr. Brian Veitch and Dr. Heather Peng.

I deeply appreciate the support of the Natural Sciences and Engineering Research Council (NSERC) of Canada, the Virtual Marine Technology (VMT), the Mathematics of Information Technology and Complex Systems (MITACS) and the Graduate Fellowship from Memorial University. Without their financial support, this work could not be possibly completed.

Many thanks are extended to my colleagues at the Advanced Marine Hydrodynamics Lab (AMHL). Finally, I would like to give my special thanks to my parents, Chengxin Guo and Xueqing Zheng. I am profoundly grateful for their love, support and understanding.

## **Abstract**

Based on the Kramer-Kronig relations, the frequency-domain added mass and damping coefficients are transformed to the time-domain added mass and response function by applying a semi-analytical method (Cao, 2008) which has significant improvement over the conventional methods, such as the Fast Fourier Transform (FFT) method. In this thesis, with the assumption of infinite depth water, heave added mass and damping coefficients of a floating hemisphere, a Wigley hull and a Liquefied Natural Gas (LNG) carrier have been computed by using the Motion Analysis Program Suite (MAPS), a program based on the panel-free method for the accurate computation of wave-body interactions in the frequency-domain. Validation studies are presented by comparing the response function based on the frequency-domain solutions by a semi-analytical method with the solutions of Qiu (2001). The accuracy of the method is also demonstrated by comparing the recovery of added mass and damping based on the computed response functions.

# Chapter 1

## Introduction

### 1.1 Response Function

Accurate computation of motions of a floating structure or a ship is very important to real-time simulation in marine applications. Currently, the linear radiation-diffraction theory is widely employed in computing the wave induced load on the structure. It is time-consuming to directly solve the boundary-value problem of the radiation and diffraction problems in the time domain, especially for a long-time simulation on a personal computer. Thus, this method is not desirable for real time simulations.

The impulse response function method, developed by Cummins (1962), introduced an effective way to solve this problem. Based on the linear radiation-diffraction theory, the wave load can be expressed in terms of hydrodynamic coefficients, such as the wave excitation forces, added mass and damping coefficients. The geometry of the underwater portion of the structure, the mode of motion and the frequency of the wave are the parameters influencing these hydrodynamic coefficients. For a given hull, the hydrodynamic coefficients need

only to be calculated once, and the results can then be stored as a database. The database includes the wave excitation force transfer functions and the second-order wave drift force transfer functions for carefully selected wave frequencies and directions and the added mass and radiation damping coefficients for the six degrees of freedom of motion. With the employment of the database, the wave loads on the structure undergoing six degrees of freedom of motion can be calculated repeatedly in various environmental conditions in either the frequency-domain or the time-domain calculations. The response function, which is also called the retardation function, is desired in the calculation of the corresponding radiation/diffraction wave load in the time-domain.

The concept of the direct time-domain solution is based on the early work of Finkelstein (1957), Stoker (1957) and Wehausen and Laitone (1960). In the work of Cong, *et al.* (1998) and Qiu (2001), the response function is determined by solving an integral equation directly in the time-domain at each time step. To enhance the capability of the combined formulation, a pseudo-nonlinear scheme was developed by Qiu *et al.* (2001). In that work, varied hydrodynamic coefficients for various waterlines were considered. The time-domain added mass, damping and restoring force coefficients were pre-computed for various wetted surfaces by choosing hull attitudes. When the wetted surface of the hull varies during the time-domain computation, these coefficients are interpolated at the instantaneous wetted surface at each time interval. This method showed

promising improvements for motion prediction, particularly for roll. However, panelizing the hull for various positions required additional efforts.

Another approach to compute the response function is to solve the problem indirectly based on the frequency-domain solution. The added mass and damping coefficients, together with the time-domain added mass and the response function, are related through the Kramer-Kronig relations over the entire frequency range. For a floating structure which has general geometry, it is usually easier to obtain the added mass and damping coefficients in the frequency domain.

## **1.2 The Computation of Added Mass and Damping Coefficients**

The panel method has been widely used to calculate the velocity and force distribution along the surface of a ship and offshore structure's under water portion. Hess and Smith (1964) first developed the panel method in which the geometry of the hull was divided into flat panels. All the panels on the hull influence each other and all the influences are collected in a matrix. In addition, a flow condition, which must be satisfied by the induced velocities, is defined on the underwater portion of the hull surface.

A panel-free method has been developed by Qiu and Hsiung (2001) and Qiu *et al.* (2006). They have first applied the panel-free method to wave interactions with bodies in the time domain and then in the frequency domain. In their studies, the singularity which is caused by the Rankine term in the Green function was removed and the desingularized integral equations were first developed. The Non-Uniform Rational B-Splines (NURBS) were employed to represent the exact body surface mathematically. The conventional integral equations were then discretized over the hull surface by the use of Gaussian quadrature. The results of the panel-free method have been demonstrated by its applications to simple geometry bodies such as submerged spheres, hemispheres, vertically floating cylinders and Wigley hulls. In this work, the Motion Analysis Program Suite (MAPS), based on the panel-free method, is employed to compute the added mass and damping coefficients in the frequency domain.

### **1.3 The Computation of Response Function from Frequency-Domain Results**

The added mass and damping coefficients can be transformed to the time-domain added mass and response function according to the Kramer-Kronig relations. Conventional numerical quadrature can be employed to evaluate the integrals over the sub-domains. However, numerical quadrature is likely to give inaccurate and unreliable results due to the nature of the method. Moreover,

great computational efforts are required by the higher-order quadratures. The response function can also be obtained by employing the Fast Fourier Transform (FFT) method which can overcome the disadvantages of conventional quadrature. However, the FFT method will also have high computational cost. A highly accurate semi-analytical integration method was introduced by Cao (2008) to evaluate the integrals for the time-domain added mass and response functions. Since this method does not suffer the numerical difficulties and high computational costs, it has significant improvements over the conventional method and the FFT method.

## **1.4 Thesis Contents**

The purpose of the thesis is to develop an efficient numerical tool to calculate the time-domain response functions of ships based on the frequency-domain added mass and damping coefficient. Based on the Kramer-Kronig relations, the time-domain response functions are obtained by transforming the frequency-domain added mass and damping coefficients using a semi-analytical method (Cao, 2008). A computer program, Motion Analysis Program Suite (MAPS) based on the panel-free method, was employed to compute the frequency-domain added mass and damping coefficients.

In this thesis, the theoretical background of the panel-free method is presented in Chapter 2. Chapter 3 describes an improved transformation method for the response function computation. The mathematical formulation and the numerical

method are introduced. The conventional methods, such as the numerical quadrature and the FFT method are also described. The validation studies for a hemisphere, a Wigley hull and a Liquefied Natural Gas (LNG) carrier are presented in Chapter 4. The response functions computed by the semi-analytical method were compared with those by the FFT method. Conclusions are drawn in Chapter 5.

## Chapter 2

# The Panel-Free Method for Frequency Domain Computation

The MAPS has been developed by Qiu *et al.* (2006) based on the panel-free method for the accurate computation of wave-body interactions in the frequency domain. In the panel-free method developed by Qiu (2001) and Qiu *et al.* (2006), modified nonsingular integral equations were first developed. The Gaussian points were distributed over the exact body surface, and also were automatically distributed on the interior free surface. In comparison with panel method, the advantages of panel-free method have been shown to be:

- a) Less numerical manipulation, since panelization of a hull surface is no longer needed.
- b) Greater accuracy, since the assumption for the degree of approximation of source strength distribution which made in the panel method is not needed and the surface geometry can be mathematically described.
- c) The integral equation is desingularized before it is discretized so that Gaussian quadrature can be applied directly and globally. In the panel method, the singularity remains in the discretized integral equation and Gaussian

quadrature cannot be applied directly over the body surface.

- d) The Gaussian quadrature points, and their respective Jacobian and normals on the surface can be accurately computed based on the NURBS expression; The NURBS surface can be obtained directly from commercial computer aided design packages.
- e) The accuracy of the solution can be easily controlled by changing the number and/or the arrangement of Gaussian quadrature points.

The theoretical background of the panel-free method is summarized in the following sections.

## 2.1 Mathematical Formulation

A Cartesian coordinate system  $O-xyz$ , as shown in Fig 2-1, is employed to compute the wave interaction with a floating structure at zero speed. The mean wetted surface is denoted by  $S_b$ . The  $oxy$  plane is on the plane with  $z=0$  which represents the undisturbed water surface. The  $z$ -axis is positive upward.

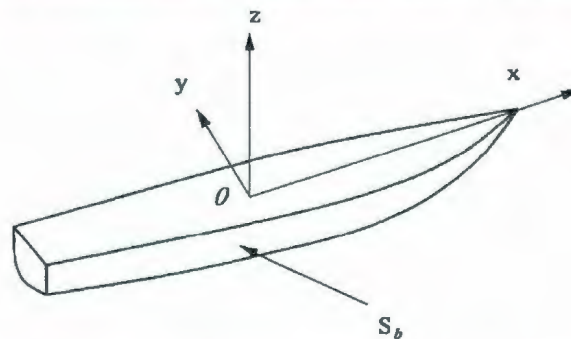


Fig 2-1 Coordinate system

Incident waves with a radial frequency  $\omega$ , spread with an angle  $\beta$  to the  $x$ -axis. The velocity potential at a field point  $P(x, y, z)$  in the fluid domain  $\Omega$  satisfies the Laplace equation and the linearized free surface boundary condition on  $z=0$ .

$$\begin{aligned}
 \nabla^2 \phi &= 0, \quad \text{in } \Omega \\
 \frac{\partial \phi}{\partial z} - \frac{\omega^2}{g} \phi &= 0, \quad \text{on } z=0 \\
 \frac{\partial \phi}{\partial n} &= V_n \quad \text{on } S_b \\
 \nabla \phi &\rightarrow 0 \quad \text{as } R_1 \rightarrow \infty, \text{ on } z=0 \\
 \nabla \phi &\rightarrow 0 \quad \text{as } z \rightarrow -\infty
 \end{aligned} \tag{2.1}$$

where  $S_b$  is the wetted surface of a body in the equilibrium position,  $V_n$  is the normal velocity,  $g$  is the acceleration of gravity. The velocity potential can be decomposed as

$$\phi(P) = \phi_R(P) + \phi_D(P) + \phi_I(P) \tag{2.2}$$

where  $\phi_R$ ,  $\phi_D$  and  $\phi_I$  are the radiation, diffraction and incident wave velocity potential, respectively. For a rigid body with six degrees of freedom, the

radiation potential can be expressed as

$$\phi_R(P) = -i\omega \sum_{k=1}^6 \xi_k \phi_k \quad (2.3)$$

where  $\xi_k$  is the complex amplitude of the body motion in the  $k$ th mode.

Introducing  $\phi_7 = \phi_D$  the radiation and the diffraction potentials can be calculated

by solving the desingularized integral equations as follows (Qiu *et al.*, 2006):

$$\begin{aligned} \phi_k(P) = & \int_{S_b} G_0(P, Q) \left[ \sigma_k(Q) - \gamma(Q) \frac{\sigma_k(P)}{\gamma(P)} \right] dS + \phi_0 \frac{\sigma_k(P)}{\gamma(P)} \\ & + \int_{S_b} \sigma_k(Q) G_F(P, Q) dS \quad k = 1, 2, 3, \dots, 7 \end{aligned} \quad (2.4)$$

where  $Q(x', y', z')$  is the source point,  $\sigma_k$  is the source strength,  $\gamma(P)$  is the source distribution on the body wetted surface  $S_b$ , and  $\phi_0$  is equipotential due to  $\gamma(P)$ . The solution of  $\phi_0$  can be found in Qiu and Hsiung (2002) and the solution of  $\sigma_k$  can be solved from the following equation (Qiu *et al.*, 2006):

$$\begin{aligned} \frac{\partial \phi_k(P)}{\partial n_P} = & -\sigma_k(P) + \int_{S_b} \left[ \sigma_k(Q) \frac{\partial G_0(P, Q)}{\partial n_P} - \sigma_k(P) \frac{\partial G_0(P, Q)}{\partial n_Q} \right] dS \\ & + \int_{S_b} \frac{\partial G_F(P, Q)}{\partial n_P} \sigma_k(Q) dS \end{aligned} \quad (2.5)$$

where

$$G_0(P, Q) = -\frac{1}{4\pi} \left( \frac{1}{r} + \frac{1}{r_1} \right), \quad (2.6)$$

$$r = \sqrt{(x-x')^2 + (y-y')^2 + (z-z')^2}, \quad (2.7)$$

and

$$r_1 = \sqrt{(x-x')^2 + (y-y')^2 + (z+z')^2}. \quad (2.8)$$

For infinite water depth

$$G_F(P, Q) = -\frac{1}{2\pi} \int_0^\infty \frac{1}{\mu - K} e^{\mu(z+z')} J_0(\mu R') d\mu - i \frac{1}{2} K e^{K(z+z')} J_0(KR') \quad (2.9)$$

with

$$R' = \sqrt{(x-x')^2 + (y-y')^2} \quad (2.10)$$

and the first-order deep-water dispersion relationship is given as

$$K = \omega^2 / g \quad (2.11)$$

where  $J_0$  is the Bessel function of zeroth order.

A modified non-singular integral equation was also developed by Qiu *et al.* (2005) to remove the effects of irregular frequencies. The body boundary condition on the interior free surface is

$$\frac{\partial \phi_k(P)}{\partial n_p} = 0 \quad \text{for } P \in S_i \quad (2.12)$$

where the  $n_p$  is the normal vector pointing into the interior free surface.

The velocity potential on the body surface  $S_b$  can be computed by

$$\begin{aligned} \phi_k(P) = & \int_{S_b} G_0(P, Q) \left[ \sigma_k(Q) - \gamma(Q) \frac{\sigma_k(P)}{\gamma(P)} \right] dS + \phi_0 \frac{\sigma_k(P)}{\gamma(P)} \\ & + \int_{S_b} \sigma_k(Q) G_F(P, Q) dS + \int_{S_i} \sigma_k(Q) G(P, Q) dS \quad \text{for } P \in S_b \quad (2.13) \end{aligned}$$

Using Gaussian quadrature with the Gaussian point as the collocation point, the desingularized integral equations can be discretized over exact surfaces,  $S_b$  and  $S_i$ .

## 2.2 Geometry Representation

Since the desingularized integral equations can be discretized over exact

geometry by applying Gaussian quadrature, accurately computing coordinates, normals and Jacobians of Gaussian points becomes the next important task. Non-uniform rational B-Splines (NURBS) are employed to describe the geometry of the body surface mathematically.

Non-uniform rational B-Splines (NURBS) have become the preferred method in body surface constructions. The widespread acceptance and popularity of NURBS has resulted from the fact that they provide a common mathematical form for the precise representation of standard analytical shapes, such as conics, circles, line, and quadratic surfaces, as well as free-form curves and surfaces. NURBS offer extra degrees of freedom to generate a large variety of shapes. The method's intrinsic characteristics of local control and low memory requirement, coupled with a stable and efficient generating algorithm, make it a powerful geometric tool for surface description, especially for complicated body geometry.

In the work of Qiu (2001) and Qiu *et al.* (2006), it is assumed that  $N_p$  patches are adopted to describe a body surface. For example, for a ship with a flat transom, two patches could be used to represent the hull surface, one for the main hull and another one for the transom. Each patch can be described by a NURBS surface. Assume that  $P(x(u,v), y(u,v), z(u,v))$  is a point on a NURBS surface, where  $x$ ,  $y$  and  $z$  denote the Cartesian coordinates, and  $u$  and  $v$

are two parameters for the surface definition. On the NURBS surface,  $P(u, v)$  can be defined as

$$P(u, v) = \frac{\sum_{i=0}^n \sum_{j=0}^m w_{ij} C_{i,j} N_{i,p}(u) N_{j,q}(v)}{\sum_{i=0}^n \sum_{j=0}^m w_{ij} N_{i,p}(u) N_{j,q}(v)} \quad (2.14)$$

where  $w_{ij}$  are the weights; the  $C_{i,j}$  form a network of control points; and  $N_{i,p}(u)$  and  $N_{j,q}(v)$  are the normalized B-Spline basis functions of degrees  $p$  and  $q$  in the  $u$ - and  $v$ - directions, respectively.

Then the unit normal vector can be obtained from

$$n = n_p / |J| \quad (2.15)$$

Introducing a computational space  $rs$  which is from -1 to 1, the Gaussian quadrature points are then arranged in the  $rs$  space. The mapping relationship of the computational space  $rs$ , the parametric space  $uv$  and the physical space  $xyz$  is illustrated in Figure 2-2.

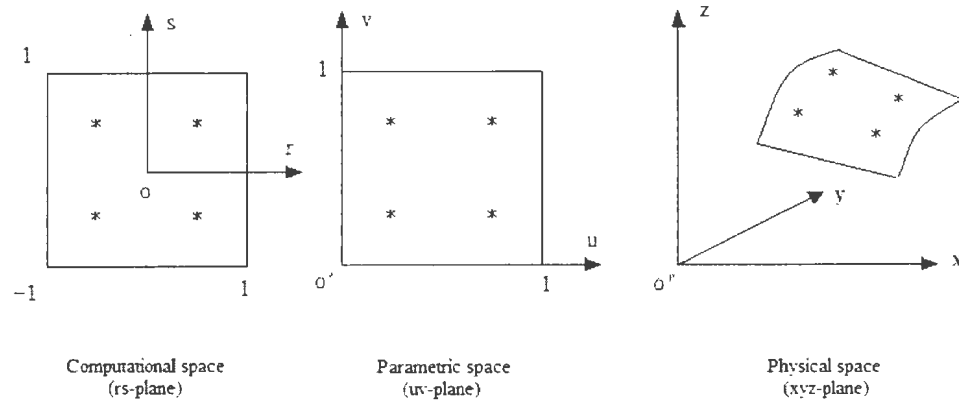


Fig 2-2 Mapping relationship for the computational space, the parametric space and the physical space (Qiu, 2001)

## Chapter 3

# Improved Transformation Method for Response Function Computation

### 3.1 Mathematical Formulation

With the assumptions of the potential flow, absence of a current, linear waves and linear motions of the structure, the wave load acting on the hull of a floating body can be expressed by the superposition of the wave exciting force and the radiation force as (Cao, 2008):

$$F(t) = F^{(w)}(t) + F^{(r)}(t) \quad (3.1)$$

where  $F(t)$  is a time ( $t$ ) dependent vector with six components. The first three are the forces along the coordinate axes and the other three are the forces about the coordinate axes. The wave exciting force  $F^{(w)}(t)$  which acts on the hull is caused by incident waves. The radiation load on the hull  $F^{(r)}(t)$  is caused by the motions of the hull in the absence of the incident waves and can be expressed as

$$F^{(r)}(t) = -\mu\ddot{x}(t) - \int_0^{\infty} K(\tau)\dot{x}(t-\tau)d\tau \quad (3.2)$$

where  $x(t)$ ,  $\dot{x}(t-\tau)$  and  $\ddot{x}(t)$  are the motion, velocity and acceleration of the hull, respectively,  $\mu$  is the time-domain added mass, a six by six constant matrix, and  $K(\tau)$  is also a six by six matrix dependent on time  $\tau$  and is called response function (or retardation function). For a steady harmonic motion of the hull with frequency  $\omega$ , the motion vector can be expressed in complex form as

$$x(t) = Xe^{-i\omega t} \quad (3.3)$$

where  $X$  is the motion amplitude of the hull. Substituting Eq. (3.3) into Eq. (3.2), we have

$$F^{(r)}(t) = \left( \omega^2 \mu + i\omega \int_0^{\infty} K(\tau) e^{i\omega\tau} d\tau \right) X e^{-i\omega t} \quad (3.4)$$

According to the work of Cao (2008),  $F^{(r)}(t)$  can also be expressed in the following form

$$F^{(r)}(t) = \left( \omega^2 A(\omega) + i\omega B(\omega) \right) X e^{-i\omega t} \quad (3.5)$$

where  $A(\omega)$  and  $B(\omega)$  are the frequency-domain added mass and damping, respectively. Both of them are six by six matrices. Comparing the right-hand side of Eq. (3.4) with that of Eq. (3.5) and applying the Euler transformation,

$$e^{ix} = \cos x + i \sin x ,$$

the following relationships can be obtained:

$$B(\omega) = \int_0^{\infty} K(\tau) \cos(\omega\tau) d\tau \quad (3.6)$$

$$\mu = A(\omega) + \frac{1}{\omega} \int_0^{\infty} K(\tau) \sin(\omega\tau) d\tau \quad (3.7)$$

As seen from Eq. (3.6),  $B(\omega)$  and  $K(\tau)$  are a cosine transform pair. Therefore,  $K(\tau)$  can be expressed in terms of  $B(\omega)$

$$K(\tau) = \frac{2}{\pi} \int_0^{\infty} B(\omega) \cos(\omega\tau) d\omega \quad (3.8)$$

Eq. (3.6) and Eq. (3.7) are one of different forms of the Kramer-Kronig relations relating  $A(\omega)$  and  $B(\omega)$  according to the work of Wehausen (1971) and

Ormberg (2004). From Eq. (3.7), it is easy to see that  $\mu = A(\infty)$  and therefore the time-domain added mass  $\mu$  is also referred to as the added mass at infinite frequency.

In this work, the frequency-domain added mass  $A(\omega)$  and damping  $B(\omega)$  are obtained by using the Motion Analysis Program Suite (MAPS) based on the panel-free method. Then, the time-domain added mass  $\mu$  and response function  $K(\tau)$  are calculated base on the Kramer-Kronig relations as given in Eq. (3.7) and Eq. (3.8).

It should be noted that, time-domain added mass  $\mu$  should be a constant matrix independent of  $\omega$ , even though the terms in the right-hand-side of Eq. (3.7) are functions of  $\omega$ . This important property of  $\mu$  is used to assess the quality of  $A(\omega)$  and  $B(\omega)$ , as well as the accuracy of the integration method used for the evaluation of  $\mu$  and  $K(\tau)$ . Let  $\tilde{A}(\omega)$ ,  $\tilde{B}(\omega)$  and  $\tilde{K}(\tau)$  be the approximation to  $A(\omega)$ ,  $B(\omega)$  and  $K(\tau)$ , respectively,

$$\tilde{K}(\tau) = \frac{2}{\pi} \text{num} \left( \int_0^{\infty} \tilde{B}(\omega) \cos(\omega\tau) d\omega \right) \quad (3.9)$$

where  $\text{num} \left( \int_0^{\infty} \tilde{B}(\omega) \cos(\omega\tau) d\omega \right)$  represents a numerical evaluation of the

integral  $\int_0^{\infty} \tilde{B}(\omega) \cos(\omega\tau) d\omega$ . Introducing  $\tilde{\mu}$  as the approximation to  $\mu$ , then

$$\tilde{\mu}(\omega) = \tilde{A}(\omega) + \frac{1}{\omega} \text{num} \left( \int_0^{\infty} \tilde{K}(\tau) \sin(\omega\tau) d\tau \right) \quad (3.10)$$

As discussed before,  $\mu$  should be a constant matrix independent of  $\omega$ . However, the values of  $\tilde{\mu}(\omega)$  will vary with  $\omega$  because of numerical errors. For a practical time-domain calculation, an averaged value  $\bar{\mu}$  derived from  $\tilde{\mu}(\omega)$  is usually used. In this study, the averaged value which minimizes the least square difference was chosen,

$$\varepsilon = \int_0^{\omega_{\max}} (\tilde{\mu}(\omega) - \bar{\mu})^2 d\omega. \quad (3.11)$$

In the perfect situation of  $\varepsilon = 0$ ,  $\tilde{\mu}(\omega)$  is independent of  $\omega$ , i.e.  $\tilde{\mu}(\omega) = \bar{\mu}$ . Therefore,  $\varepsilon$  can be used to measure the scattering of  $\tilde{\mu}(\omega)$ , and the quality of  $\tilde{A}(\omega)$  and  $\tilde{B}(\omega)$ , as well as  $\bar{\mu}$  and  $\tilde{K}(\tau)$ .

### 3.2 Numerical Method

For the integrals in Eq. (3.8), the entire frequency range  $(0, \infty)$  is first divided

into a series of sub-domains. Eq. (3.8) are expressed in terms of the sum of integrals over  $N+1$  sub-domains  $(\omega_n, \omega_{n+1})$  and  $(\omega_{N+1}, \infty)$  ( $n=1, 2, \dots, N$ ). Then, the integrals over the sub-domains are approximated by summing

$$\tilde{K}(\tau) \approx \sum_{n=1}^N \Delta \tilde{K}_n(\tau) + \Delta \tilde{K}^\infty(\tau) \quad (3.12)$$

where

$$\Delta \tilde{K}_n(\tau) = \frac{2}{\pi} \text{num} \left( \int_{\omega_n}^{\omega_{n+1}} B(\omega) \cos(\omega\tau) d\omega \right) \quad (3.13)$$

$$\Delta \tilde{K}^\infty(\tau) = \frac{2}{\pi} \text{num} \left( \int_{\omega_{N+1}}^{\infty} \tilde{B}(\omega) \cos(\omega\tau) d\omega \right). \quad (3.14)$$

In most engineering practice, a large number of sub-domains is used, and the radiation damping  $B(\omega)$  of the sub-domain  $(\omega_{N+1}, \infty)$  is sufficiently small, so the contribution from  $(\omega_{N+1}, \infty)$  is usually ignored.

The integrals in Eq. (3.6) and Eq. (3.7) can be evaluated in a similar way by swapping the roles of  $\omega$  and  $\tau$ . Three numerical integration methods are discussed below.

### 3.2.1 Numerical quadratures

A conventional numerical quadrature can be employed to evaluate the integrals over the sub-domains as

$$\Delta \tilde{K}_n(\tau) = \sum_{m=1}^M w_m \tilde{B}(\omega_{n,m}) \cos(\omega_{n,m} \tau) \quad (3.15)$$

where  $\omega_{n,m}$  is the  $m^{\text{th}}$  evaluation points of the numerical quadrature for the  $n^{\text{th}}$  segment,  $w_m$  is the weight corresponding to the evaluation point and  $M$  is the number of evaluation points for the  $n^{\text{th}}$  segment. The values of the added mass and damping,  $\tilde{A}(\omega)$  and  $\tilde{B}(\omega)$  are needed at the evaluation points. Similarly, the integral in Eq. (3.10) or Eq. (3.7), can be evaluated using the same numerical quadrature,

$$\begin{aligned} \tilde{\mu}(\omega) &= \tilde{A}(\omega) + \frac{1}{\omega} \text{num} \left( \int_0^{\infty} \tilde{K}(\tau) \sin(\omega \tau) d\tau \right) \\ &\approx \tilde{A}(\omega) + \frac{1}{\omega} \sum_{l=1}^L \left( \sum_{m=1}^M w_m \tilde{K}(\tau_{l,m}) \sin(\omega \tau_{l,m}) \right) \end{aligned} \quad (3.16)$$

where  $L$  is the number of time steps. Because of the nature of the sine and cosine functions, the kernels in the above integrals are highly oscillatory for large values of  $\omega$  or  $\tau$ . Numerical quadrature is likely to give inaccurate and

unreliable results, especially for large intervals and the wide variation of values of the integrals. Higher-order quadratures can overcome the problem in some degree, however it requires the computation of  $\tilde{A}(\omega)$  and  $\tilde{B}(\omega)$  at a very large number of frequencies and results in a high computational cost.

### 3.2.2 Fast Fourier Transform

As seen in Eq. (3.8),  $K(\tau)$  is the real part of the Fourier transform of  $B(\omega)$ . Therefore, the numerical result of  $\tilde{K}(\tau)$  can be obtained by employing the Fast Fourier Transform (FFT). The FFT method can overcome the disadvantages of the quadratures, such as the numerical difficulties and the inaccuracy. However, the FFT method requires the frequency discretization to be a uniform spacing which must be smaller than the sampling frequency in order to capture and transform the complete characteristics of  $\tilde{A}(\omega)$  and  $\tilde{B}(\omega)$ . Since the number of frequencies is large, the FFT method will have a high computational cost.

In addition, there is a further difficulty with the FFT. To obtain convergent results, the inverse Fourier transform has to be cut off at a certain frequency. The appropriate cut-off frequency for a given mode varies for different hull forms and forward speeds, and can only be determined by numerical experiments.

### 3.2.3 Semi-analytical method

A semi-analytical method is introduced by Cao (2008) to accurately evaluate the integrals. This technique does not suffer the numerical difficulties and high computational costs of numerical quadrature and FFT methods. It does not require the frequency discretization to be uniform. This significantly reduces the number of frequencies which are needed to compute  $\tilde{A}(\omega)$  and  $\tilde{B}(\omega)$ , and thus greatly enhances the computational efficiency.

Observation has shown that, compared with  $\tilde{B}(\omega)\cos(\omega\tau)$ ,  $\tilde{B}(\omega)$  is a relatively slow varying function of  $\omega$  over the entire frequency range. To numerically approximate the slow varying function  $\tilde{B}(\omega)$  is easier and better than approximating the highly oscillatory function  $\tilde{B}(\omega)\cos(\omega\tau)$ . Instead of approximating the whole integrand  $\tilde{B}(\omega)\cos(\omega\tau)$  with a polynomial in numerical quadrature, the semi-analytical method approximates  $\tilde{B}(\omega)$  with a linear function within sub-domain  $(\omega_n, \omega_{n+1})$  by

$$\tilde{B}(\omega) \approx P_1 + P_2\omega \quad (3.17)$$

where

$$P_1 = \frac{\tilde{B}(\omega_n)\omega_{n+1} - \tilde{B}(\omega_{n+1})\omega_n}{\omega_{n+1} - \omega_n}; \quad P_2 = \frac{\tilde{B}(\omega_{n+1}) - \tilde{B}(\omega_n)}{\omega_{n+1} - \omega_n} . \quad (3.18)$$

The contribution to the response function on the sub-domain  $(\omega_n, \omega_{n+1})$  can then be expressed as

$$\Delta \tilde{K}_n(\tau) \approx \int_{\omega_n}^{\omega_{n+1}} (P_1 + P_2 \omega) \cos(\omega \tau) d\omega = P_1 J_1 + P_2 J_2 \quad (3.19)$$

where

$$J_1 = \int_{\omega_n}^{\omega_{n+1}} \cos(\omega \tau) d\omega \quad (3.20)$$

And

$$J_2 = \int_{\omega_n}^{\omega_{n+1}} \omega \cos(\omega \tau) d\omega. \quad (3.21)$$

The analytically results for the integrals in Eq. (3.20) and Eq. (3.21) can be easily obtained as

$$J_1 = \frac{1}{\tau} (\sin(\omega_{n+1} \tau) - \sin(\omega_n \tau)) \quad (3.22)$$

$$\text{and } J_2 = \frac{1}{\tau} \left( \omega_{n+1} \sin(\omega_{n+1} \tau) - \omega_n \sin(\omega_n \tau) + \frac{1}{\tau} (\cos(\omega_{n+1} \tau) - \cos(\omega_n \tau)) \right). \quad (3.23)$$

The contribution on range  $(\omega_{N+1}, \infty)$  can also be accounted. Since  $\tilde{B}(\omega)$  should vanish as  $\omega \rightarrow \infty$ , it can be approximated with an exponentially decaying function as

$$\tilde{B}(\omega) \approx \alpha e^{-\beta(\omega-\omega_{N+1})} \quad (3.24)$$

where  $\beta$  is a positive number in order for  $\tilde{B}(\omega)$  to vanish as  $\omega \rightarrow \infty$ .  $\alpha$  and  $\beta$  are determined so that  $\tilde{B}(\omega)$  and its first derivative are continuous at  $\omega_{N+1}$ , in which case

$$\alpha = \tilde{B}(\omega_{N+1}) \quad (3.25)$$

$$\beta = \frac{-1}{\tilde{B}(\omega_{N+1})} \frac{d\tilde{B}(\omega_{N+1})}{d\omega} \quad (3.26)$$

The first derivative  $\frac{d\tilde{B}(\omega_{N+1})}{d\omega}$  can be approximated by using finite differencing.

The contribution from range  $(\omega_{N+1}, \infty)$  can be then expressed by

$$\begin{aligned} \Delta K^\infty(\tau) &= \int_{\omega_{N+1}}^{\infty} \tilde{B}(\omega) \cos(\omega\tau) d\omega \approx \alpha \int_{\omega_{N+1}}^{\infty} e^{-\beta(\omega-\omega_{N+1})} \cos(\omega\tau) d\omega \\ &= \alpha \frac{\beta \cos(\omega_{N+1}\tau) - \tau \sin(\omega_{N+1}\tau)}{\beta^2 + \tau^2} \end{aligned} \quad (3.27)$$

The semi-analytical method can also be used to evaluate the radiation damping  $B(\omega)$  and time-domain added mass  $\mu$  (the integrals in Eq. (3.6) and Eq. (3.7)) by simply swapping the roles of  $\omega$  and  $\tau$ .

### 3.2.4 Accuracy check of the integration method

Since  $B(\omega)$  and  $K(\tau)$  are a transform pair in Eq. (3.6) and Eq. (3.8), these equations can be used to check the accuracy of the numerical integration. The response function  $\tilde{K}(\tau)$  is computed first. Then, Eq. (3.7) and Eq. (3.6) are used to calculate the approximation of time-domain added mass  $\tilde{\mu}(\omega)$  and the reconstructed damping  $\tilde{\tilde{B}}(\omega_n)$ . According to Cao's work (2008), the error criterion to assess the quantity of  $\tilde{\mu}(\omega)$  is given as

$$\tilde{\varepsilon} = \int_0^{\omega_{N+1}} (\tilde{\mu}(\omega) - \bar{\mu})^2 d\omega / \int_0^{\omega_{N+1}} (\bar{\mu})^2 d\omega . \quad (3.28)$$

The smaller  $\tilde{\varepsilon}$  is, the closer  $\tilde{\mu}(\omega)$  is to the constant  $\bar{\mu}$ .

The relative least-squared difference between  $\tilde{\tilde{B}}(\omega_n)$  and  $\tilde{B}(\omega_n)$ , which used to measure the closeness, is given as

$$\delta = \int_0^{\omega_{N+1}} (\tilde{\tilde{B}}(\omega) - \tilde{B}(\omega))^2 d\omega / \int_0^{\omega_{N+1}} (\tilde{B}(\omega))^2 d\omega . \quad (3.29)$$

The closer  $\tilde{\tilde{B}}(\omega_n)$  is to  $\tilde{B}(\omega_n)$ , the better the accuracy of the integration.

In addition, the time-domain added mass  $\mu$  should be a constant matrix which is independent of  $\omega$  even though the individual terms in the right-hand-side of Eq. (3.7) are functions of  $\omega$ .

The calculation procedure is summarized as follows:

- 1) Compute added mass  $\tilde{A}(\omega)$  and damping  $\tilde{B}(\omega)$  by using MAPS at a set of frequencies.
- 2) Calculate the retardation functions  $\tilde{K}(\tau)$ , the time-domain added mass  $\tilde{\mu}(\omega)$  and its average  $\bar{\mu}$  by the semi-analytical method.
- 3) Reconstruct the added mass and radiation damping using the Kramer-Kronig relations,

$$\tilde{A}(\omega) = \bar{\mu} - \frac{1}{\omega} \int_0^{\infty} \tilde{K}(\tau) \sin(\omega\tau) d\tau \quad (3.30)$$

$$\tilde{B}(\omega) = \int_0^{\infty} \tilde{K}(\tau) \cos(\omega\tau) d\tau \quad (3.31)$$

- 4) Calculate the error

$$\tilde{\epsilon} = \int_0^{\omega_{N+1}} (\tilde{\mu}(\omega) - \bar{\mu})^2 d\omega / \int_0^{\omega_{N+1}} (\bar{\mu})^2 d\omega \quad (3.28)$$

and the relative least-difference between  $\tilde{B}(\omega_n)$  and  $\tilde{B}(\omega_n)$

$$\delta = \int_0^{\omega_{N+1}} (\tilde{B}(\omega) - \tilde{B}(\omega))^2 d\omega / \int_0^{\omega_{N+1}} (\tilde{B}(\omega))^2 d\omega \quad (3.29)$$

## Chapter 4

### Numerical results

The added mass and damping of a floating hemisphere, a Wigley hull and a Liquefied Natural Gas (LNG) carrier was computed by using MAPS based on the panel-free method. The frequency-domain results can then be employed to calculate the response function using the Kramer-Kronig relations. The numerical results of the hemisphere and the Wigley hull were compared with the time-domain solutions by Qiu (2001).

#### 4.1 Hemisphere

A hemisphere with a radius  $R=10.0m$  is floating in deep water. The body surface of the hemisphere was represented by NURBS surfaces. In the NURBS representation, the hemisphere was described by four NURBS surfaces. Each NURBS surface is formed by a  $4 \times 4$  control net and B-Splines of degrees of 3 in the  $u$ - and  $v$ - directions. The number of Gaussian points over a quarter of the hemisphere is chosen as  $8 \times 8$ . To remove irregular frequencies, the Gaussian points on the interior free surface  $S_i$  are automatically distributed according to

the geometry of the waterline.

#### 4.1.1 The added mass and damping coefficients

Fig 4-1 and Fig 4-2 present the added mass and damping coefficients versus the non-dimensional frequency for the hemisphere in heave. In these figures, the frequency, computed heave added mass and radiation damping coefficient are nondimensionalized as  $\omega^2 R/g$ ,  $A_{33}/(\rho \nabla)$  and  $B_{33}/(\rho \nabla \omega)$ , respectively, where  $\rho$  is the water density and  $\nabla$  is the volume displacement.

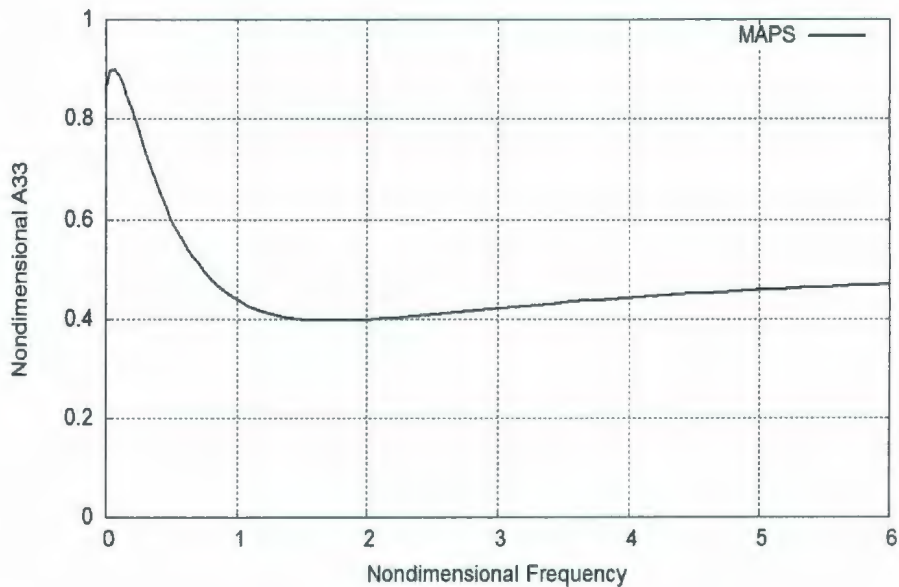


Fig 4-1 Heave added mass for the hemisphere

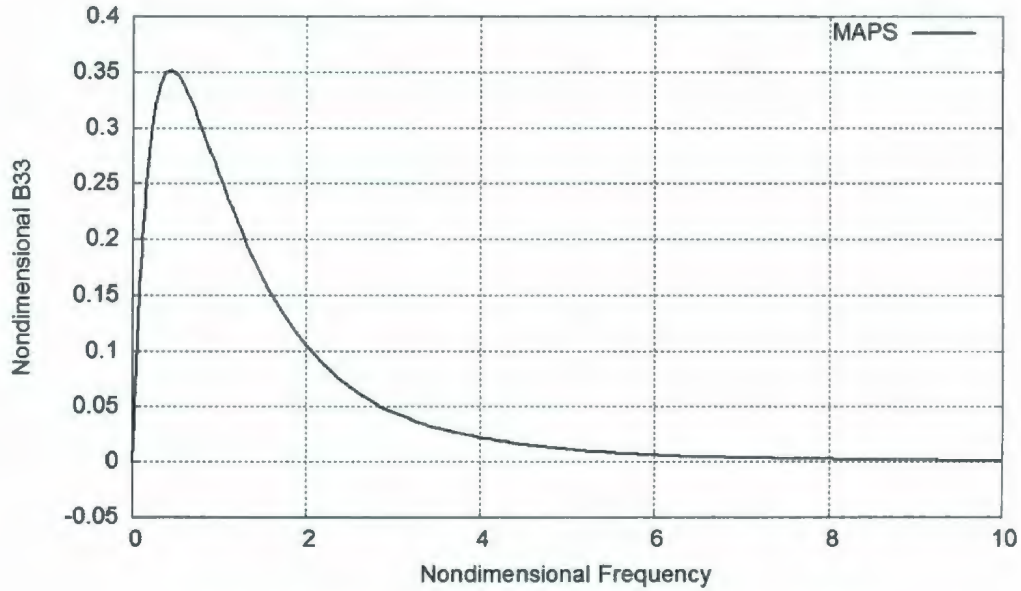


Fig 4-2 Heave damping coefficient for the hemisphere

#### 4.1.2 Response function

The semi-analytical method and the FFT method were applied to compute the heave response function for the hemisphere. The results by the semi-analytical method and the FFT method are compared with the time-domain solution by the panel-free method (Qiu, 2001) in Figure 4-3. The time and heave response function are nondimensionalized as  $t\sqrt{g/R}$  and  $K_{33}(t)/(\rho\nabla)\sqrt{R/g}$ , respectively, where  $R$  is the radius of the hemisphere. The time step,  $dt$ , was chosen as 0.02 second. At the same time step,  $dt$ , the results from the semi-analytical method showed a good agreement with the time-domain solution by the panel-free method and those by the FFT method.

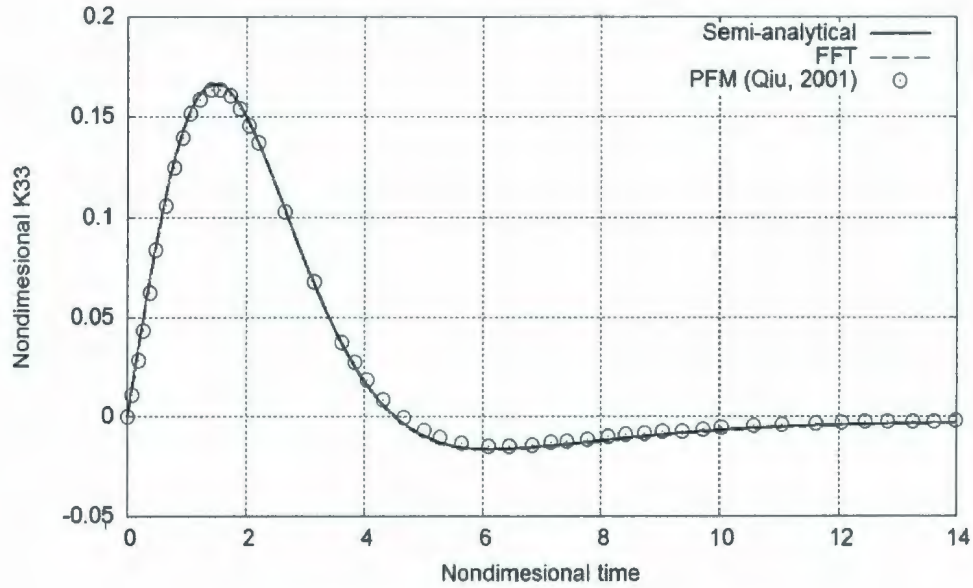


Fig 4-3 Heave response function for the hemisphere

#### 4.1.3 Accuracy check of the integral method

Since  $K(\tau)$  and  $B(\omega)$  are a transfer pair, the recovery of the damping coefficient based on the computed response function can be used to check the accuracy of the integral method. The recovered heave damping coefficient, the recovered heave added mass and the time-domain added mass are presented in Fig 4-4 to Fig 4-6. As seen, the recovery of the heave damping coefficient and added mass are in good quality and the time-domain added mass  $\mu(\omega)$  is barely dependent on  $\omega$ .

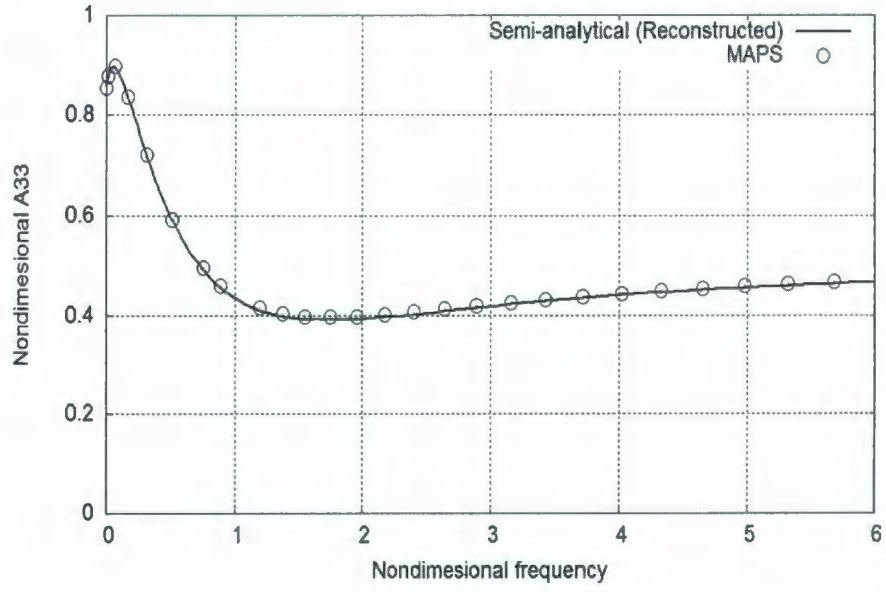


Fig 4-4 Reconstructed heave added mass for the hemisphere

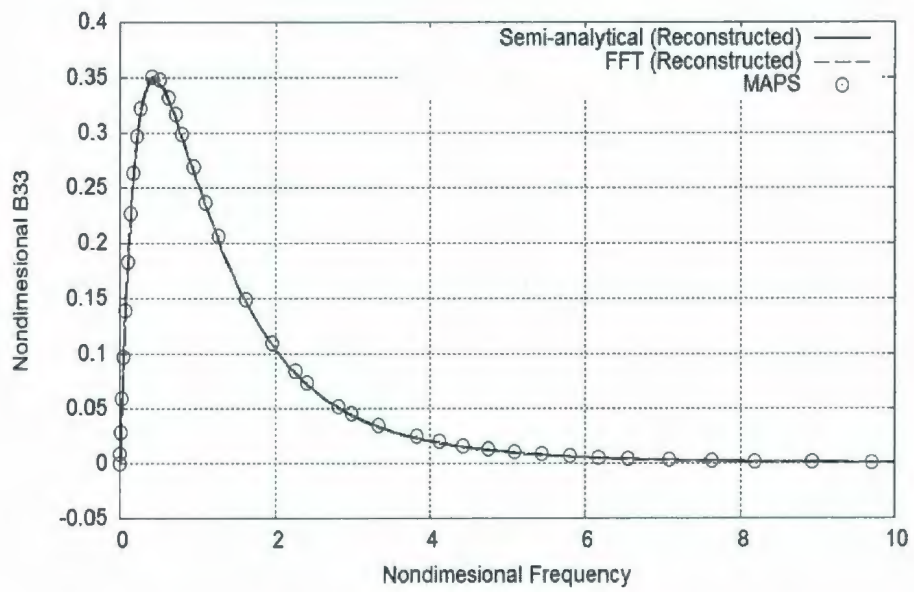


Fig 4-5 Reconstructed heave damping coefficient for the hemisphere

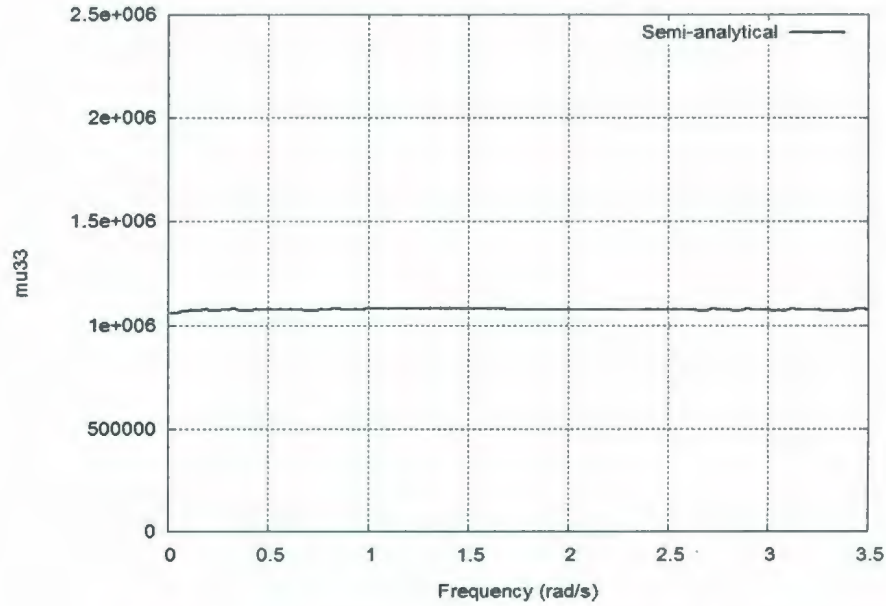


Fig 4-6 Time-domain heave added mass for the hemisphere

## 4.2 Wigley Hull

Heave added mass and damping coefficients have also been computed for a Wigley-hull ship at zero speed in water of infinite depth by using MAPS.

The hull geometry is defined by (Journée, 1992)

$$\eta = (1 - \zeta^2)(1 - \xi^2)(1 + 0.2\xi^2) + \zeta^2(1 - \zeta^8)(1 - \xi^2)^4 \quad (4.1)$$

where the nondimensional variables are given by

$$\xi = 2x/L, \quad \eta = 2y/B, \quad \zeta = z/T \quad (4.2)$$

where  $L$  is the length of the Wigley hull,  $B$  is the beam and  $T$  is the draft.

The hull has

$$L/B = 10, \quad L/T = 16, \quad L = 120.0 \quad (4.3)$$

and a block coefficient of

$$C_b = \frac{\nabla}{LBT} = 0.5606 \quad (4.4)$$

NURBS representations were used for the computation. In the NURBS expression, the half Wigley hull was described by a  $13 \times 13$  control net with degrees of 3 in both  $u$ - and  $v$ - directions. In the computation,  $41 \times 10$  and  $21 \times 4$  Gaussian points are distributed on half of the wetted surface and on half of the interior free surface, respectively.

#### 4.2.1 Added mass and damping coefficient

Fig 4-7 shows the heave added mass and Fig 4-8 presents the heave damping coefficient. The frequency, heave added mass and radiation damping coefficient are nondimensionalized as  $\omega^2 B/g$ ,  $A_{33}/(\rho \nabla)$  and  $B_{33}/(\rho \nabla \omega)$  respectively,

where  $\rho$  is the water density and  $B$  is the beam of the Wigley hull.

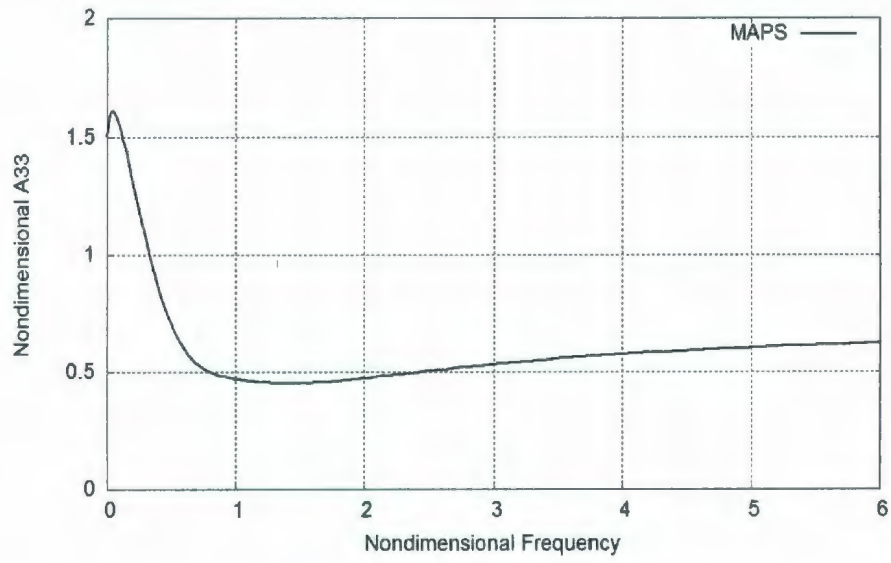


Fig 4-7 Heave added mass for the Wigley hull

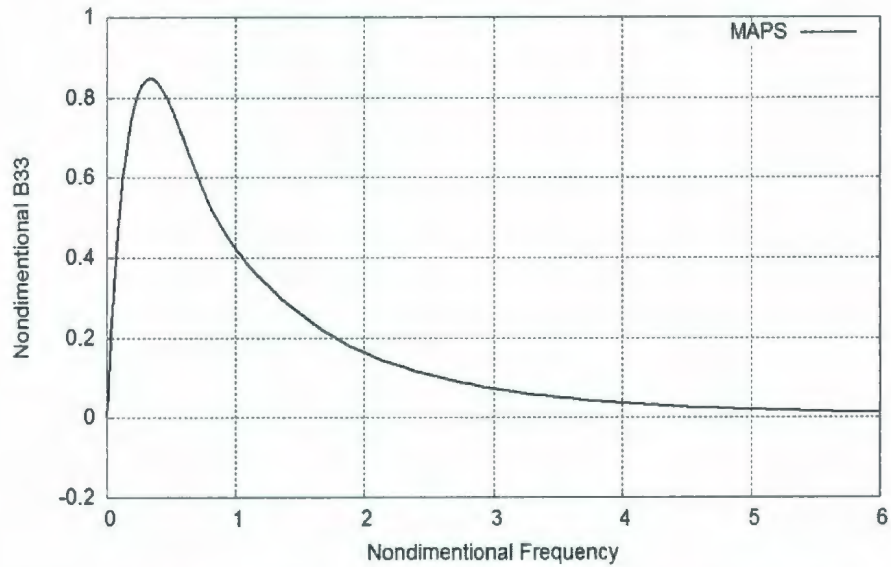


Fig 4-8 Heave damping coefficient for the Wigley hull

## 4.2.2 Response function

At a given time step  $\Delta t = 0.02s$ , the heave response function was computed by the semi-analytical method and the FFT method, respectively. The results were compared with that of the time-domain solution (Qiu, 2001). Fig 4-9 and Fig 4-10 show the computed heave response function and pitch radiation response function by using the semi-analytical method and the FFT method, respectively. In these figures, the time  $t$ , the heave response function  $K_{33}$  and the pitch radiation response function  $K_{55}$  are non-dimensionalized as  $t\sqrt{g/L}$ ,  $K_{33}\sqrt{g/L}/(\rho g \nabla/L)$  and  $K_{55}\sqrt{g/L}/(g \nabla)$  respectively, where  $L$  is the length of the Wigley hull.

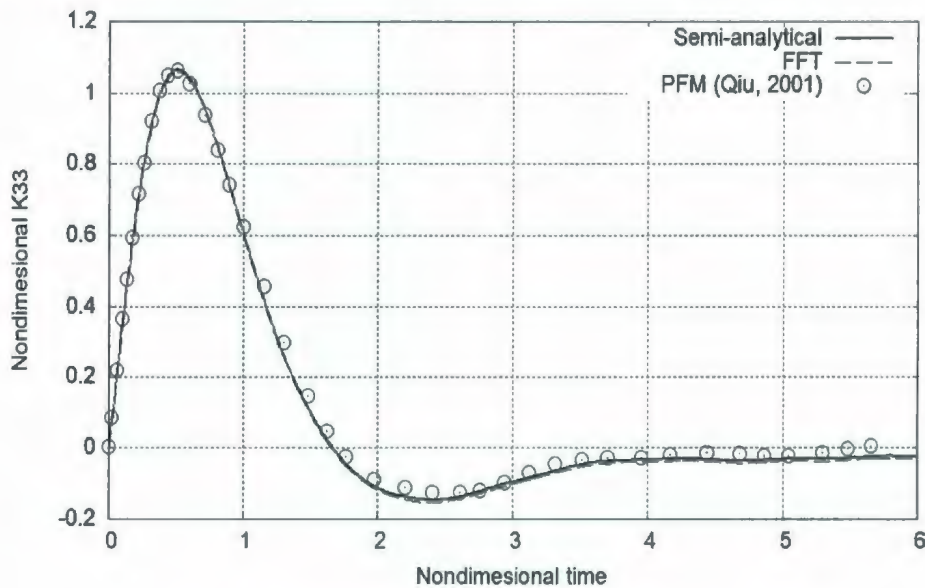


Fig 4-9 Heave response function for the Wigley hull

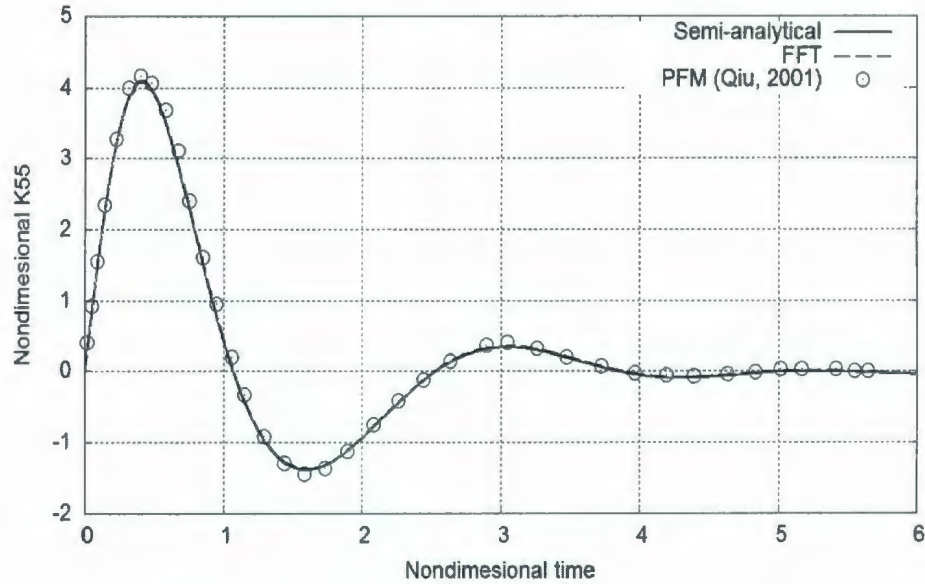


Fig 4-10 Pitch radiation response function for the Wigley hull

As presented in Fig 4-9 and Fig 4-10, the response functions computed by the semi-analytical method, the FFT method and the solution of Qiu (2001) agree with each other very well.

#### 4.2.3 Accuracy check of the integral method

The recovery of the heave damping coefficient, heave added mass and time-domain heave added mass based on the computed heave response function are presented in Fig 4-11 to Fig 4-13. As shown, the reconstructed heave damping coefficient and heave added mass by the semi-analytical method have good qualities and the time-domain heave added mass  $\mu(\omega)$  is much less dependent on  $\omega$ . It demonstrates the great accuracy of the semi-analytical

method.

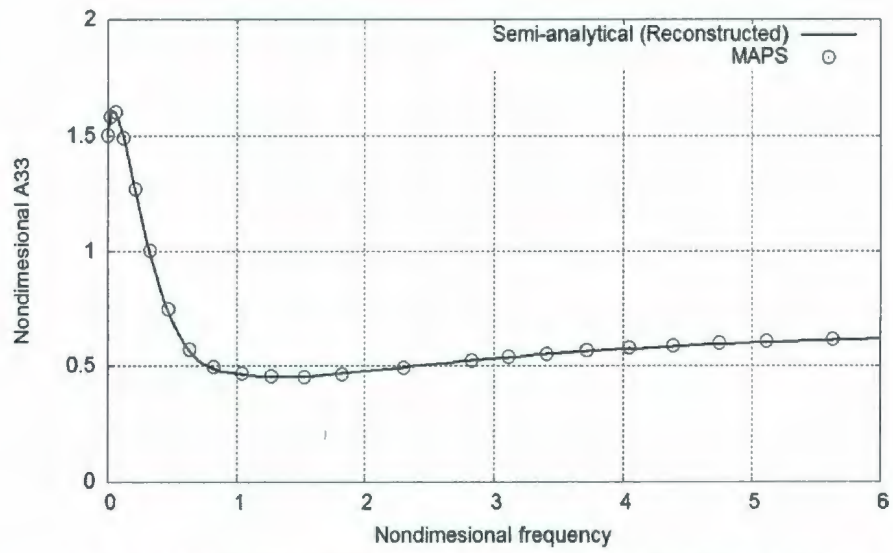


Fig 4-11 Reconstructed heave added mass for the Wigley hull

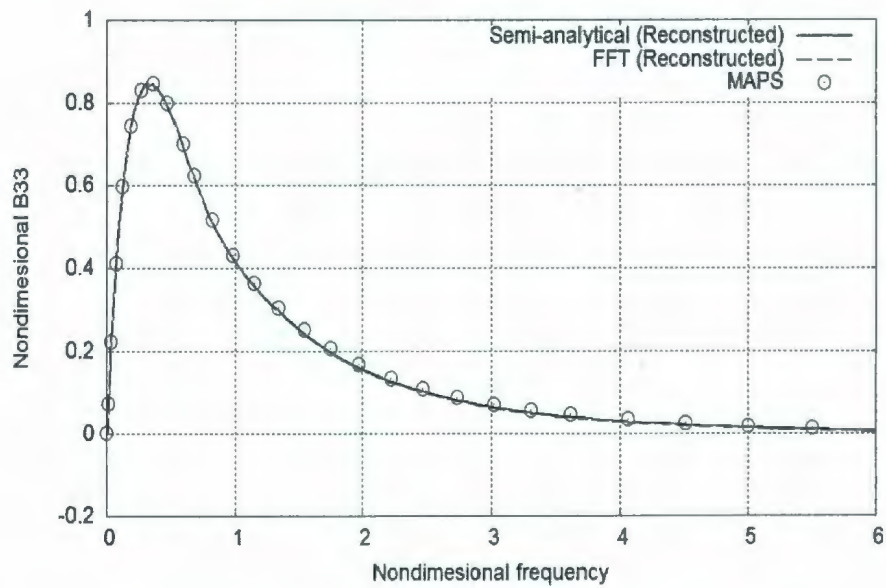


Fig 4-12 Reconstructed heave damping coefficient for the Wigley hull

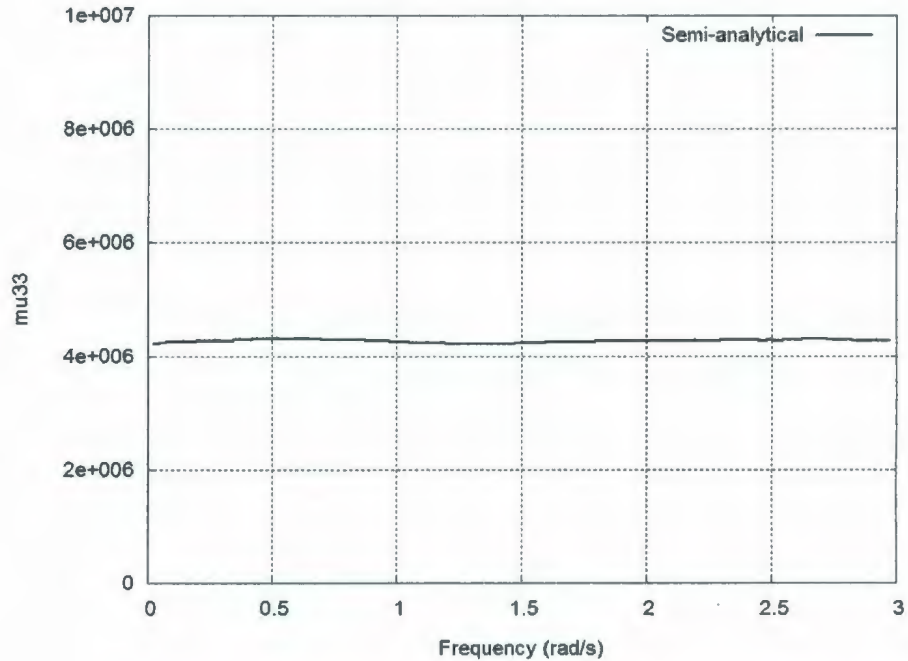


Fig 4-13 Time-domain heave added mass for the Wigley hull

### 4.3 Liquefied Natural Gas (LNG) Carrier

Heave added mass and damping coefficient have been computed by MAPS for a Liquefied Natural Gas (LNG) carrier in shallow water waves. The water depth for the LNG carrier is 15 m. Gaussian points were automatically distributed on the entire wetted surface. Fig 4-14 shows the Gaussian points on the wetted surface and on the lid. In the computation by MAPS, 4200 Gaussian points were distributed on the entire wetted surface and 1800 Gaussian points were on the lid.

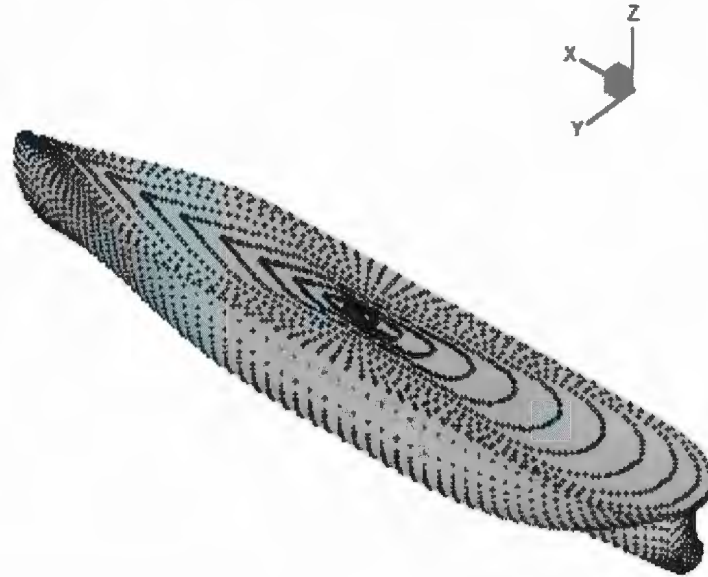


Fig 4-14 Gaussian points distribution on the hull surface and the lid of the LNG carrier (Peng *et al.*, 2007)

#### **4.3.1 Added mass and damping coefficient**

The heave added mass and the heave damping coefficient of the LNG carrier are shown in Fig 4-15 and Fig 4-16.

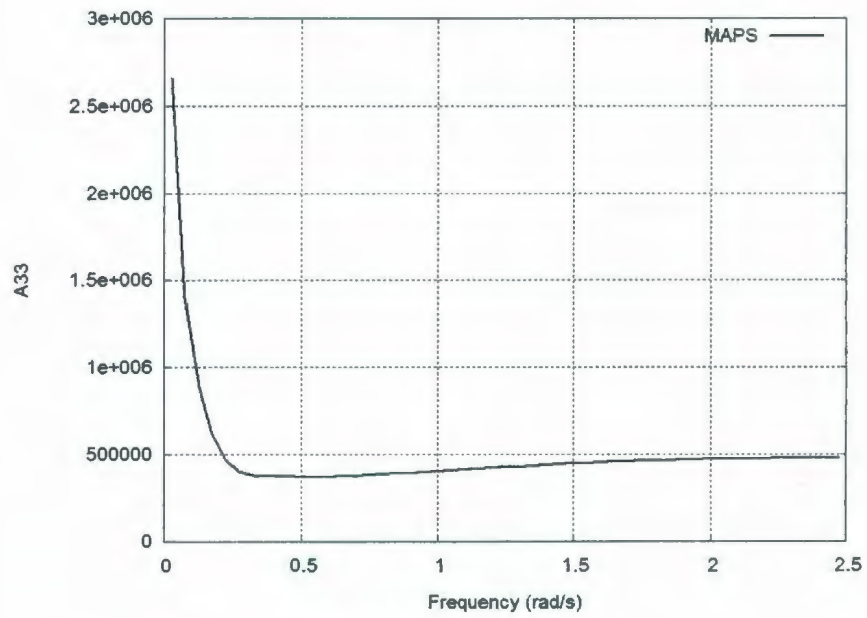


Fig 4-15 Heave added mass for the LNG carrier

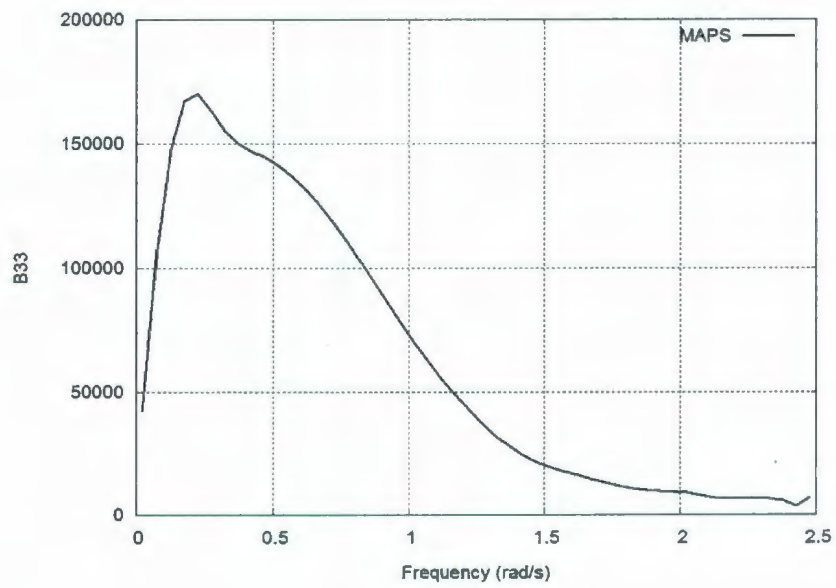


Fig 4-16 Heave damping coefficient for the LNG carrier

### 4.3.2 Response function

Fig 4-17 to Fig 4-20 show the response functions computed by the semi-analytical method and the FFT method for a time step of  $\Delta t = 0.05s$ . Obviously, the results computed by the semi-analytical method are much more reasonable than those by the FFT method in which significant peaks appear for the case when frequency interval is  $\Delta\omega = 0.05 \text{ rad/s}$ .

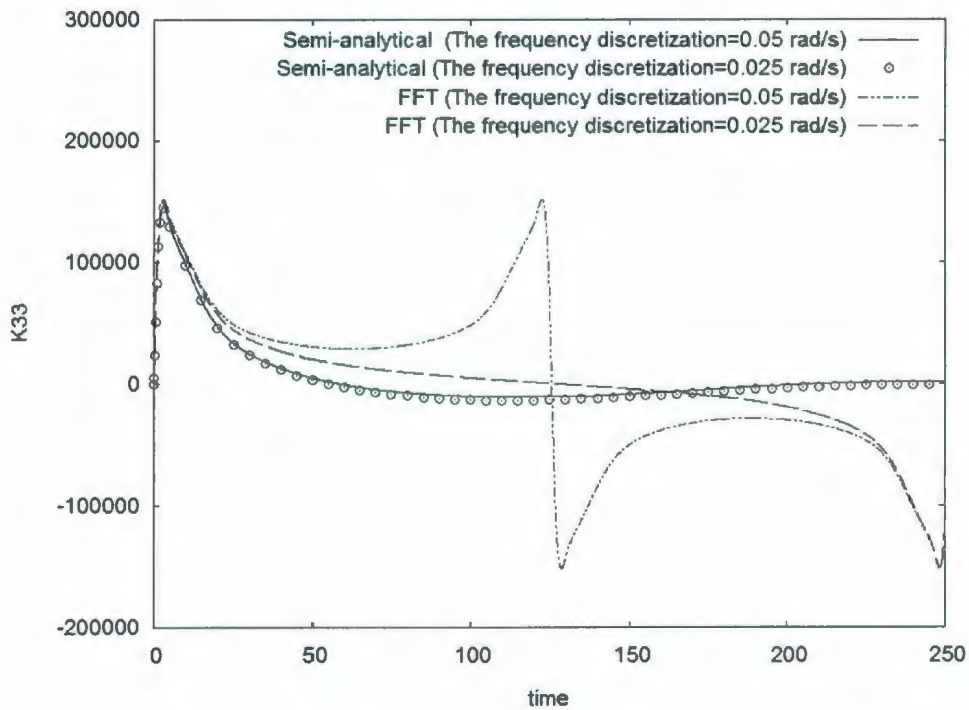


Fig 4-17 Heave response function for the LNG carrier

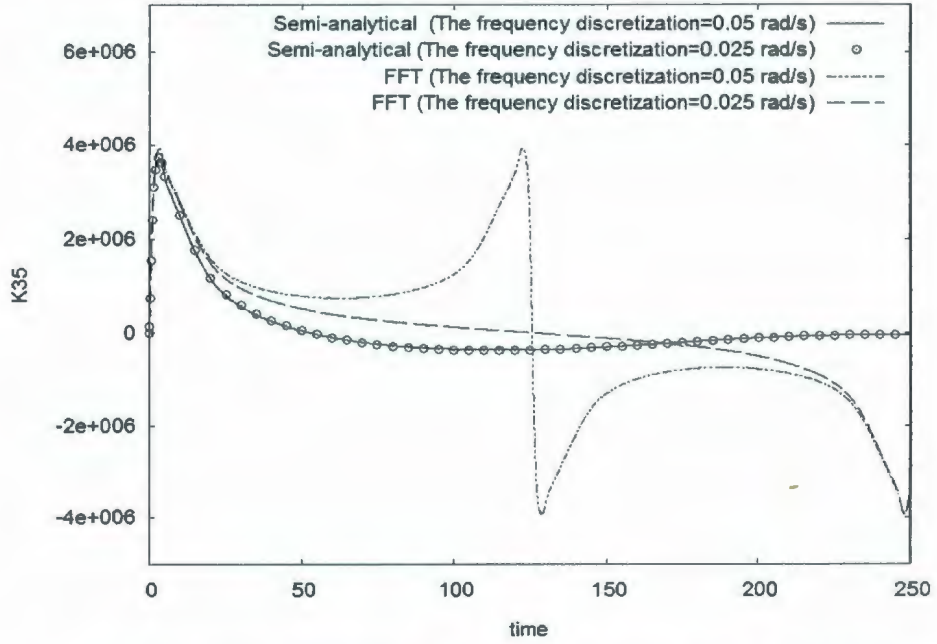


Fig 4-18 Heave response function due to pitch for the LNG carrier

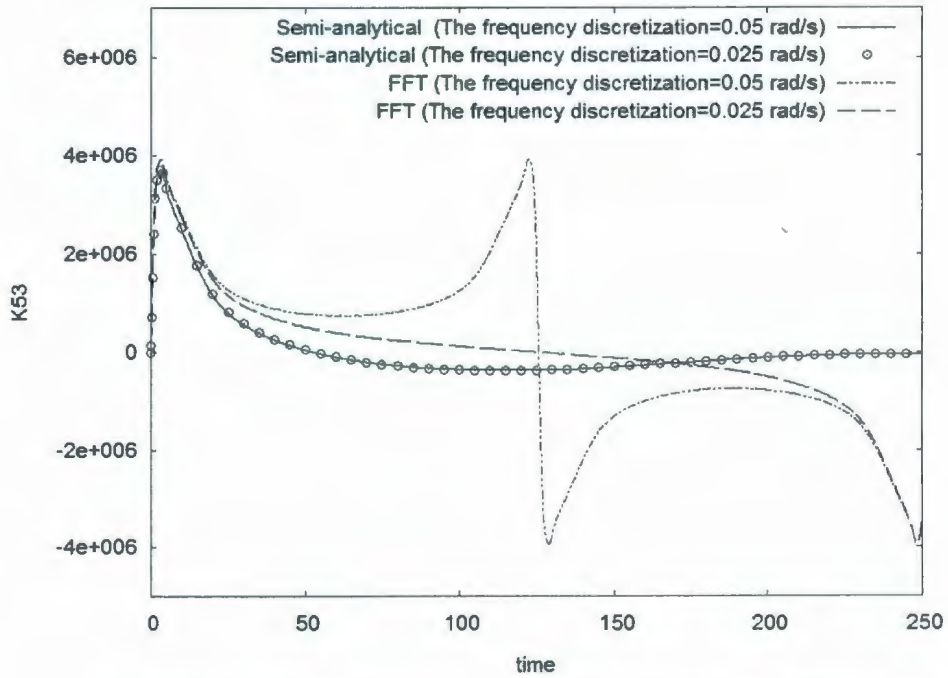


Fig 4-19 Pitch response function due to heave for the LNG carrier

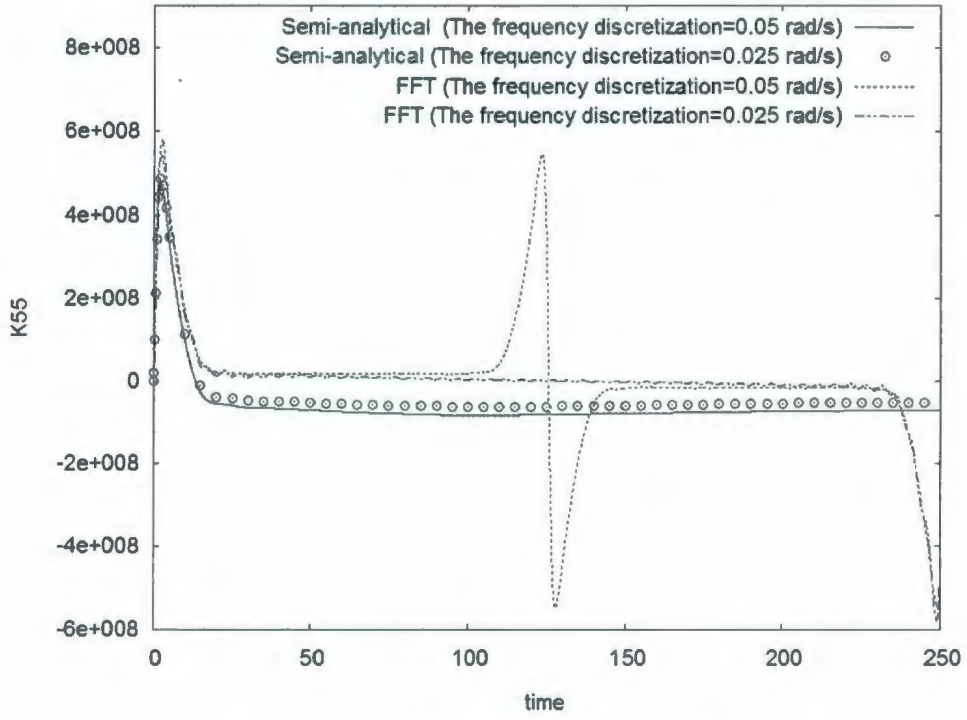


Fig 4-20 Pitch response function for the LNG carrier

### 4.3.3 Accuracy check of the integral method

Fig 4-21 to Fig 4-26 present the time-domain heave added mass, the recovery of the heave added mass and the damping coefficients base on the computed response functions. As shown, at the frequency discretization  $d\omega = 0.05 \text{ rad/s}$ , the damping coefficients by the semi-analytical method were reconstructed successfully while the results by the FFT method fail to reconstruct the original damping coefficients.

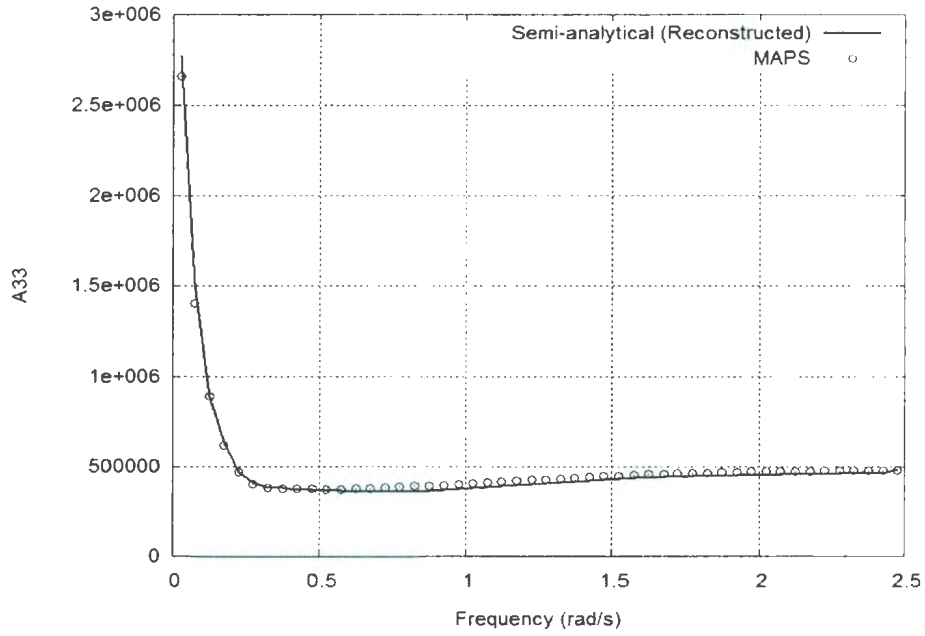


Fig 4-21 Reconstructed heave added mass for the LNG carrier

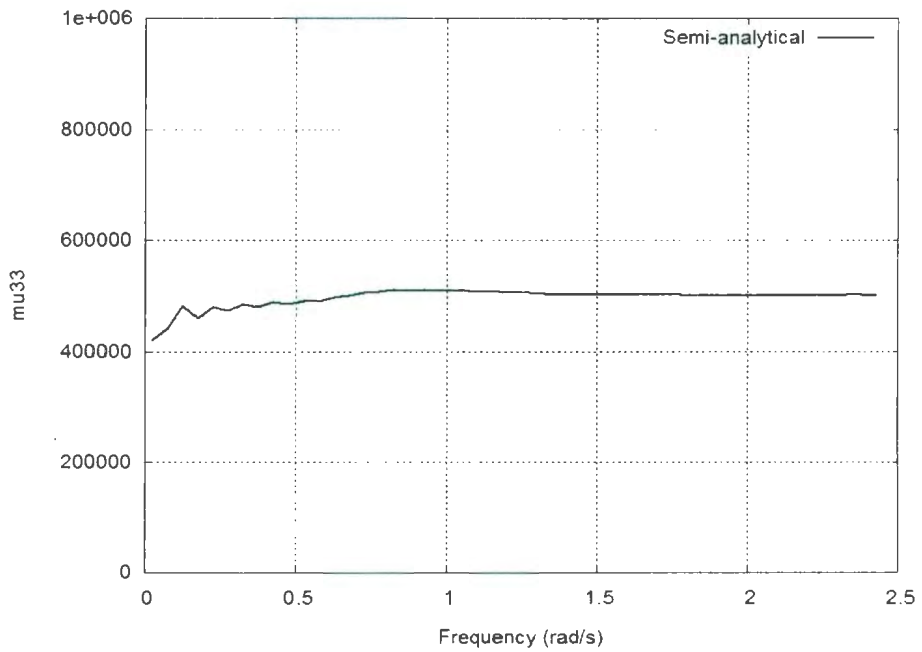


Fig 4-22 Time-domain heave added mass for the LNG carrier

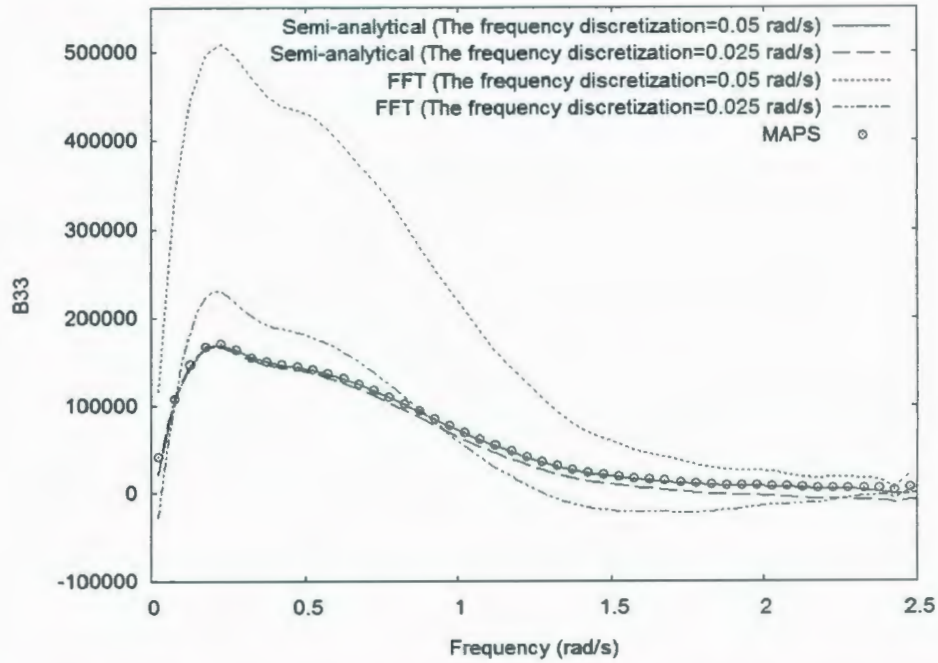


Fig 4-23 Reconstructed heave damping coefficient for the LNG carrier

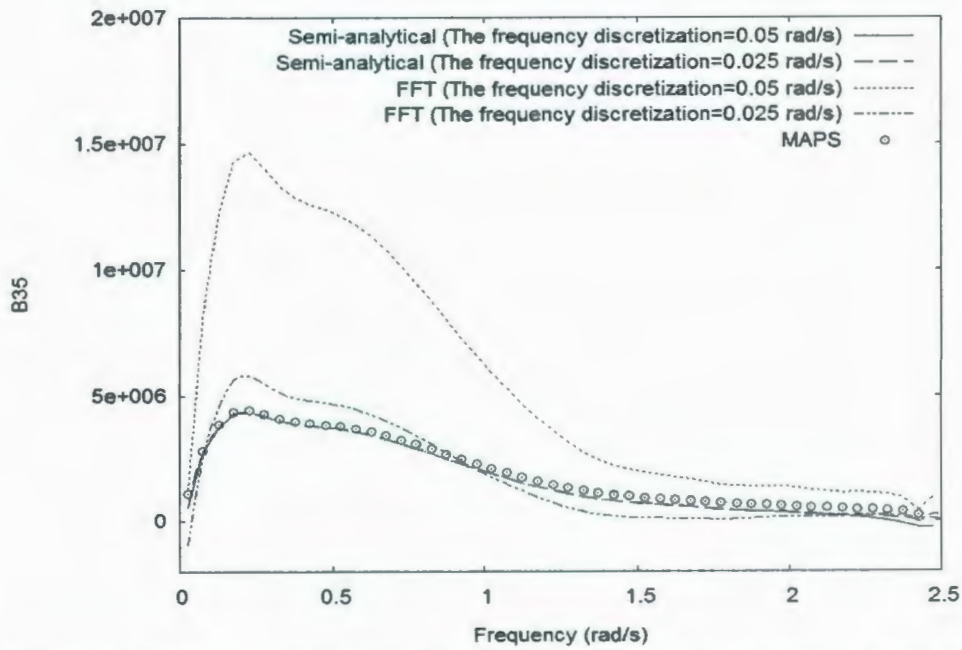


Fig 4-24 Reconstructed heave damping coefficient due to pitch for the LNG carrier

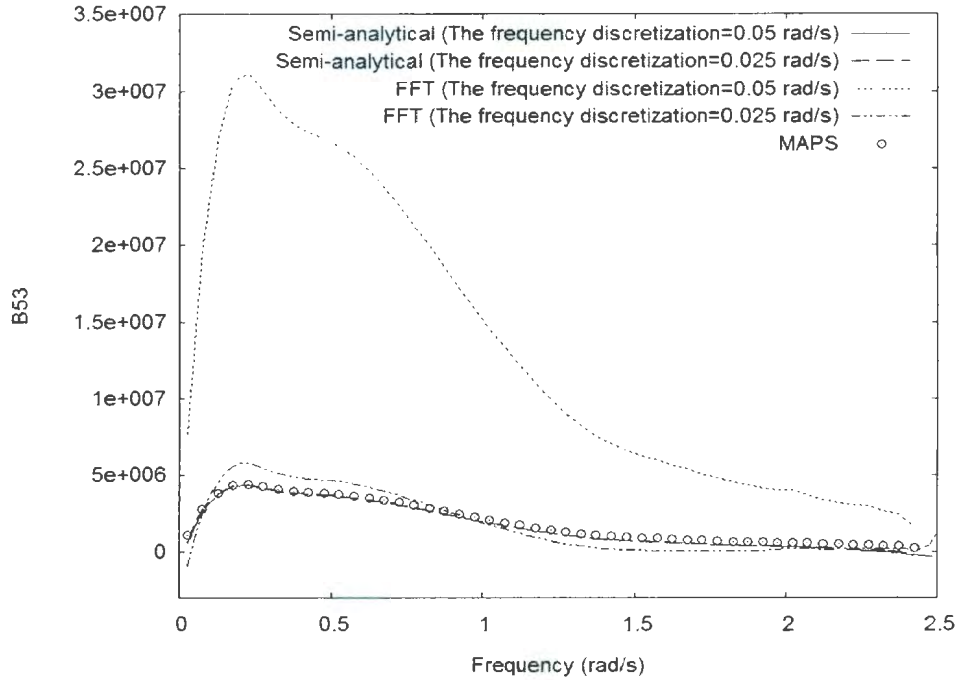


Fig 4-25 Reconstructed pitch damping coefficient due to heave for the LNG carrier

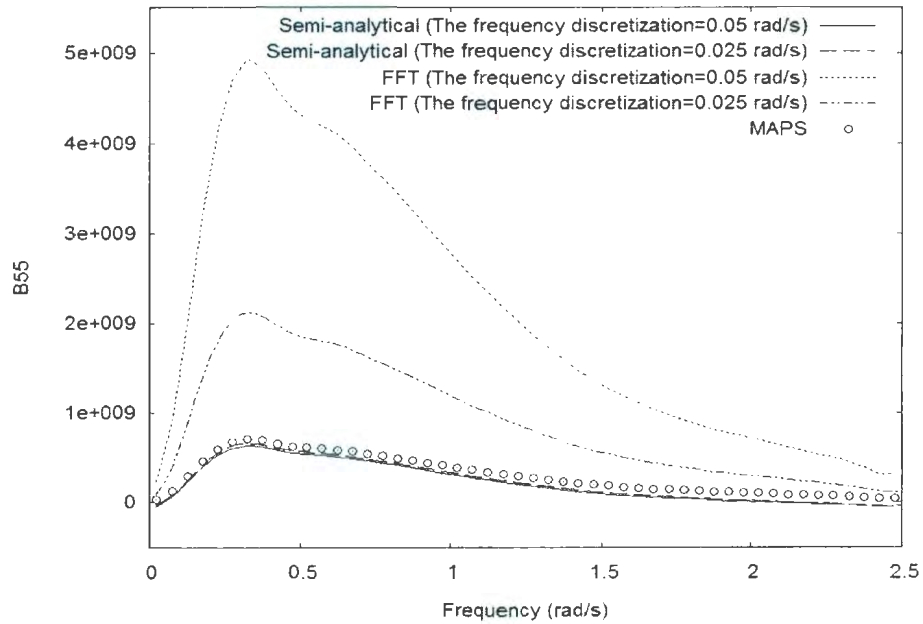


Fig 4-26 Reconstructed pitch damping coefficient due for the LNG carrier

For simple shapes (hemi-sphere and Wigley hull) both the semi-analytical method and the FFT method present very good results. However, for the complicated shape (LNG carrier), the FFT method gives unreasonable results at a large spacing of frequency discretization. The reason is the FFT method requires the spacing of the frequency discretization to be smaller than the sampling frequency in order to capture and transfer the complete characteristics of damping coefficients into response functions. To obtain reasonable results from the FFT method the frequency discretization must be refined which requires the computation of added mass and damping coefficient for a large number of frequencies. This imposes a high computational cost. Compared with the FFT method, the semi-analytical method is more accurate and efficient, especially for complicated geometry.

## **Chapter 5**

### **Conclusions**

A practical procedure is presented to evaluate, assess and improve the computation of the retardation function or response function to be stored in a database for use in the calculations of the radiation loads on a floating body. To generate a high quality database, the procedure does not require a tremendous amount of computational effort. The procedure is very suitable for practical use.

A highly accurate semi-analytical integration method was introduced for evaluation of the integrals for the time-domain response functions, as well as the integrals in the Kramer-Kronig relations.

The Motion Analysis Program Suite (MAPS) based on the panel-free method (PFM) has been employed to solve the added mass and radiation damping in the frequency domain. The Non-Uniform Rational B-Splines (NURBS) were adopted to mathematically describe the exact body geometry.

The accuracy of the semi-analytical method is demonstrated by comparing the

response functions from the frequency-domain solutions with those from the direct time-domain solutions (Qiu, 2001) for a floating hemisphere, a Wigley-hull ship in water of infinite depth. The accuracy of the method is also illustrated by comparing the recovered added mass and damping coefficients with the original ones.

The significant efficiency and accuracy of the semi-analytical method for the complicated geometry is further demonstrated by its application to an LNG carrier.

The semi-analytical method for computing response functions can be integrated into the ship motion programs in the time domain for real-time simulations.

## References

Cao, Yusong, 2008, "A Procedure for Evaluation, Assessment and Improvement of Added Mass and Radiation Damping of Floating Structures," 27<sup>th</sup> International Conference on Offshore Mechanics and Arctic Engineering 2008-57275.

Cong, L.Z., Huang, Z.J., Ando, S. and Hsiung, C.C., 1998, "Time Domain Analysis of Ship Motions and Hydrodynamic Pressures on a Ship Hull in Waves," 2<sup>nd</sup> Intn'l Conf. on Hydroelasticity in Marine Technology, Fukuoka, Japan.

Cummins, W.E., 1962, "The Impulse Response Function and Ship Motions," Schiffstechnik, Vol. 9, pp. 101-109.

Finkelstein, A. 1957, "The Initial Value Problem for Transient Water Waves" Comm. Pure App. Math., Vol. 10.

Hess, J.L. and Smith, A.M.O., 1964, "Calculation of Non-Lifting Potential Flow About Arbitrary Three-Dimensional Bodies," Journal of Ship Research, Vol. 8, No.2, pp. 22-44.

Journée, J.M.J., 1992, "Experiments and Calculations on Four Wigley Hull forms," Faculty of Mechanical Engineering and Marine Technology, Delft University of Technology, MEMT 21.

Peng, H., Qiu, W. and Spencer, D., 2007, "Validation Studies of the Panel-Free Method for Wave-Body Interaction Analysis," ISOPE 2007, Vancouver.

Qiu, W., 2001, "A Panel-Free Method for Time Domain Analysis of Floating Bodies in Waves," PhD thesis, Dalhousie University, Halifax, Nova Scotia.

Qiu, W. and Hsiung, C.C., 2002, "A Panel-Free Method for Time-Domain Analysis of Radiation Problem," *Ocean Engineering*, Vol. 29, No. 12, pp. 1555-1567.

Qiu, W., Peng, H. and Hsiung, C.C., 2005, "Removal of Irregular Frequency Effect in the Computation of Wave-Body Interactions Using the Panel-Free Method," *Oceanic Engineering International Journal*, Vol.9, No.1.

Qiu, W., Peng, H. and Chuang, J.M., 2006, "Computation of Wave-Body Interactions Using the Panel-Free Method and Exact Geometry," *Journal of Offshore Mechanics and Arctic Engineering*, Vol. 128.

Stoker, J.J., 1957, "Water Waves," International Science Publishers, Inc., New York.

Wehausen, J.V. 1971, "The Motion of Floating Bodies." *Ann. Rev. Fluid Mech.* Vol. 3, pp. 237-268.

Wehausen, J.V. and Laitone, E.V., 1960, "Surface Waves." *Handbuch der Physik*, Vol. 9, pp. 446-778, Springer-Verlag, Berlin and New York.







